Tunable THz absorbers based on LC-tuned Yagi-Uda antennas

Article *in* Liquid Crystals · April 2024

DOI: 10.1080/02678292.2024.2339913

4 authors, including:

Ivan I Yakovkin
Taras Shevchenko National University of Kyiv
41 PUBLICATIONS **69** CITATIONS
SEE PROFILE

Victor Yu. Reshetnyak
369 PUBLICATIONS **4,396** CITATIONS
SEE PROFILE

Tunable THz absorbers based on LC-tuned Yagi-Uda antennas

Ivan I. Yakovkin,[a*] Victor Yu. Reshetnyak,[a,b] Timothy J. Bunning,[c] and Dean R. Evans[c]

[a]*Physics Faculty, Taras Shevchenko National University of Kyiv, Kyiv 01601, Ukraine*

[b]*School of Physics and Astronomy, University of Leeds, Leeds LS2 9JT, United Kingdom*

[c]*Air Force Research Laboratory, Wright-Patterson Air Force Base, 45433, USA*

*email: yakovkinii@gmail.com

Tunable THz absorbers based on LC-tuned Yagi-Uda antennas

This study examines the structural configuration of Yagi-Uda micro-antenna arrays, the resonant properties of which are tunable through nematic liquid crystals in the terahertz spectral region. Reorienting liquid crystals by varying the voltage applied to the liquid crystal cell allows for control of the reflectance and absorbance amplitudes within the 7–12 THz operational frequency range. The reflectance and absorbance control ranges are around 50–60% across most of the frequency range, notably reaching approximately 90% at 11.1 THz. The optimal operational voltage ranges for the presented structure were approximately 1.1–1.9 V at the lower frequencies and 1.4–2.5 V at higher frequencies. This research highlights the potential of such metamaterial designs for efficient and adaptable applications in the THz spectrum.

Keywords: Yagi-Uda micro-antennas; nematic liquid crystals; controllable reflectance; metamaterials

Introduction

Metamaterials are a key area of exploration in recent scientific research, known for their exceptional properties such as negative refraction, cloaking, advanced lensing, dynamic tunability in plasmon-induced transparency, and perfect absorption [1–8]. What sets metamaterials apart from conventional materials is not their composition, but their intricately engineered structures [9–15]. This reliance on structure for their properties opens up possibilities for creating innovative devices [16–21] for applications in the microwave and optical regions [22–26]. Among the diverse metamaterials, perfect metamaterial absorbers (PMAs) have received substantial interest [27–29]. Advancements in research have expanded PMAs' capabilities, leading to designs that effectively function across a range of electromagnetic spectrum segments, including the microwaves, millimeter, terahertz, and visible frequencies [30–34].

In the microwave domain, configurations employing copper and iron nanowires with a

high length-to-diameter ratio have shown exceptional absorption efficiencies [35, 36]. In the terahertz spectrum, materials like graphene have been pivotal in developing effective absorbers [31]. Similarly, for the visible spectrum, the use of nanostructured elements has demonstrated the versatility of these absorbers [32, 34].

Particularly notable are antenna configurations consisting of multiple parallel elements, often referred to as Yagi-Uda structures. These structures have been recognized for their resonance and directional properties, making them suitable for achieving near-perfect absorption at specific wavelengths [37, 38]. These qualities have extended their applications beyond traditional communication systems to areas such as electromagnetic interference mitigation.

Bilal et al. [39] introduced a multiband Yagi-Uda metamaterial absorber (YUMA) that operates in the X- and Ku-bands of the microwave spectrum. It exhibited three distinct absorption peaks at 10.64 GHz, 12.08 GHz, and 14.09 GHz, demonstrating polarization control and independence of the incidence angle of the absorbed light. The study highlighted the significant role of mutual coupling in the arms of the Yagi-Uda structure in this multiband absorption process.

Integrating liquid crystals (LCs) into metamaterials significantly broadens their functional scope [40–42]. Reorientation of LCs opens possibilities for real-time tuning of resonance characteristics of the metamaterials in terms of frequency and intensity [43–45]. In [46], the Yagi-Uda metamaterial absorber's capabilities were enhanced through the integration of LCs, showing promise for dynamically manipulating antenna properties in the X- and Ku-bands to enable dynamic reconfigurability.

In our current study, we explore the tunability of 2D Yagi-Uda micro-antenna arrays using nematic LCs in the THz spectral region. We propose a structural configuration that

enables control of absorbance and reflectance up to 90% with a voltage requirement of just 2.5 Volts, illustrating the potential for highly efficient and adaptable metamaterial designs.

Structure description and problem statement

In this paper, we investigate the dynamic control and tunability of the reflectance and absorbance spectra of Yagi-Uda micro-antennas by incorporating LCs, extending the design discussed in [39, 46]. The structure under investigation consists of an infinite periodic 2D array of Yagi-Uda micro-antennas resting on a dielectric slab (Fig. 1a). A thin metal foil forming a ground plane is underneath a dielectric slab to enhance the reflectance and absorption of the Yagi-Uda antenna. The material below the ground plane has a negligible impact on the resonant properties of the antenna array; therefore, it is assumed to be a vacuum for simplicity. The Yagi-Uda micro-antennas are filled above with a nematic LC (on top of the dielectric slab), bounded on the other side by a semi-infinite glass layer.

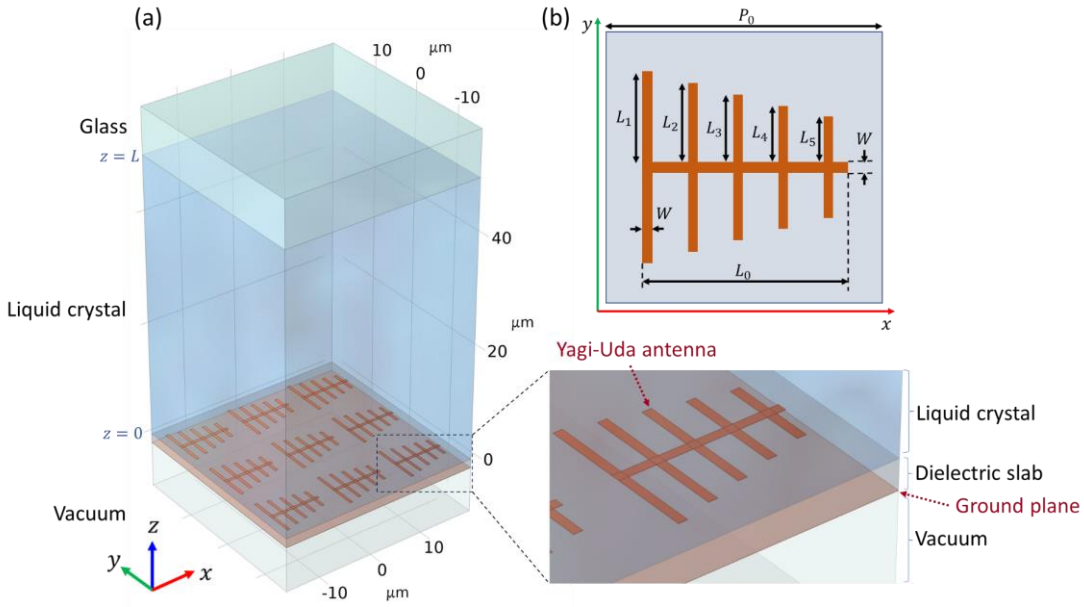

Figure 1. The structure and its enlarged fragment (a); unit cell of the Yagi-Uda micro-antenna array (b).

The normally incident y-polarized light, propagating in the negative z-direction, enters the structure from the glass medium and passes through the LC layer before reaching the Yagi-Uda antenna array. The LC director has an initial $\pi/2$ twist configuration: at the interface with glass the director is aligned along the x direction, and near the Yagi-Uda antennas the director is aligned along the y direction. This twist can be obtained by rubbing top and bottom substrates at 90-degree angles and incorporating the appropriate chiral dopant. The dimensions of the LC were chosen in a way that the Mauguin regime is established. This is achieved when $(n_e - n_o)L$ is much larger than $\lambda/4$, where L is the thickness of the LC cell, n_o and n_e are the ordinary and extraordinary refractive indexes of the LC, and λ is the wavelength in free space. This makes the initially y-polarized wave follow the director twist and reach the Yagi-Uda antennas effectively having x-polarization.

By applying an external electric field along the z direction, the LC director can be reoriented to establish a homeotropic LC cell configuration, effectively disabling the Mauguin regime. This causes the polarization of the incident wave to be polarized predominantly along the y- direction after passing through the LC layer, which in turn results in a different resonant response of the Yagi-Uda antennas. In practice, a thin layer of conducting polymer, which exhibits high transparency in the THz spectral region, can be introduced to facilitate the application of voltage [47].

Materials and dimensions

The ordinary and extraordinary indexes of the LC were chosen to be $n_o = 1.7$ and $n_e = 2.2$, respectively, corresponding to the high-birefringence LC mixtures reported in [48–49]. The LC layer thickness was chosen to be $L = 50\ \mu$m to facilitate the Mauguin regime. The refractive index of glass was also set to 1.7 to avoid additional reflections at the LC – glass interface. The Yagi-Uda antenna array and the ground plane are copper, with the real and imaginary parts of refractive indexes corresponding to those reported in [50]. The antenna consists of a base and five perpendicular arms, each having a width of 0.5 μm. Together they form the antenna of a length of $L_0 = 9\ \mu$m, with arms on both sides of the base having the lengths of 4 μm (L_1), 3.5 μm (L_2), 3 μm (L_3), 2.5 μm (L_4), and 2 μm (L_5), respectively (Fig. 1b). The thickness of the antenna and the ground plane is 35 nm. The lateral periodicity is defined by the square unit cell with the size of $P_0 = 10\ \mu$m. The dielectric slab has the thickness of 1.6 μm and is made out of a material such as flame-retardant glass epoxy FR4 [51] with a relative permittivity of 4.3 and a loss tangent of 0.025 [39]. The elastic coefficients of the LC are set to $K_{11} = 11.1 \times 10^{-12}$ N, $K_{22} = 5.9 \times 10^{-12}$ N, and $K_{33} = 17.1 \times 10^{-12}$ N, corresponding to the E7 LC mixture [52]. The LC is assumed to be lossless with the parallel and perpendicular components of the static dielectric permittivity of $\epsilon_{\parallel} = 19.28\,\epsilon_0$ and $\epsilon_{\perp} = 5.21\,\epsilon_0$, respectively [52], where ϵ_0 is the vacuum permittivity.

The numeric calculations of light absorption and propagation in the described structure were performed using the finite element method in COMSOL Multiphysics, where the spatial periodicity of the structure in the x- and y- directions was modeled by introducing Floquet periodic boundary conditions, and the semi-infinite span of the substrates in the z direction was modeled by incorporating the perfectly-matched layers.

Free energy formalism

When assessing the control range available through the reorientation of the LC, it is important to take into account that it is typically close to impossible to achieve full director reorientation at the boundaries. This aspect cannot be neglected as the plasmonic resonances are most sensitive to the dielectric functions near the areas of maximum electric field amplification, that is, in the presented case, near the arms of the Yagi-Uda antennas. In order to assess the control range, while accounting for the specified restriction, we have considered a case of rigid anchoring conditions for the director at the bounding substrates without the effects of easy axis gliding. This approach therefore corresponds to the worst-case scenario, since finite anchoring energy or easy axis gliding would likely facilitate a more complete degree of the director reorientation.

To find the director profiles, we start by considering a plane-parallel nematic LC cell bounded by the planes $z = 0$ and $z = L$. The equilibrium director profiles of the nematic LC correspond to the minimum of the free energy functional, which can be written in the form [53]:

$$F = \frac{1}{2}\int_0^L \left[f(\theta)\theta'^2 + g(\theta)\phi'^2 + K_{22}\frac{2\pi}{p}\left(\frac{2\pi}{p} - 2\cos^2\theta\right)\phi' + \epsilon_a {E_z}^2 \sin^2\theta \right] dz, \quad (1)$$

where

$$\begin{aligned} f(\theta) &= K_{11}\cos^2\theta + K_{33}\sin^2\theta\,, \\ g(\theta) &= (K_{22}\cos^2\theta + K_{33}\sin^2\theta)\cos^2\theta\,. \end{aligned} \quad (2)$$

The first two terms in (1) represent the free energy of elastic deformations of the LC, the third term takes into account the intrinsic pitch of the chiral nematic, and the last term describes the interaction between the LC and the electric field. Here, K_{11}, K_{22}, and K_{33} are the coefficients of elastic deformations of the LC, p is the intrinsic chiral pitch, E_z is z-component of the local electric field strength vector, ϵ_a is the static dielectric

anisotropy of the LC, θ and ϕ denote the director angles:

$$\vec{n} = (\cos\theta\cos\varphi\,, \cos\theta\sin\varphi\,, \sin\theta).$$

Primes denote derivatives with respect to the z-coordinate. We consider the rigid anchoring conditions (strong anchoring) at the boundaries $z = 0$ and $z = L$:

$$\begin{aligned} \theta\big|_{z=0} &= \theta_0, \\ \theta\big|_{z=L} &= \theta_0, \\ \phi\big|_{z=0} &= \frac{\pi}{2}, \\ \phi\big|_{z=L} &= 0. \end{aligned} \tag{3}$$

The pre-tilt angle $\theta_0 = 1°$ ensures that the director reorientation within the LC does not have a threshold, allowing for a more gradual response of the director angles to the changes in the applied voltage. The free energy functional minimization with respect to the distributions $\theta(z)$ and $\phi(z)$ of the director angles has to be performed, while taking into account the equations of electrostatics $\operatorname{div}\vec{D} = 0$ and $\operatorname{curl}\vec{E} = 0$ and the corresponding boundary conditions. Accounting for $\hat{\epsilon} = \epsilon_\perp\hat{1} + \epsilon_a\vec{n}\otimes\vec{n}$, the electrostatic equations take the form:

$$\begin{aligned} &\vec{E} = -\vec{\nabla}\Phi \\ &\frac{d}{dz}[(\epsilon_\perp + \epsilon_a\sin^2\theta)\Phi'] = 0, \end{aligned} \tag{4}$$

with the following boundary conditions

$$\begin{aligned} \Phi\big|_{z=0} &= 0, \\ \Phi\big|_{z=L} &= U, \end{aligned} \tag{5}$$

where U is the potential difference applied to the cell. The minimization of the free energy yields the Euler-Lagrange equations:

$$\theta'' f + \frac{1}{2}\theta'^2 f'_\theta - \frac{1}{2} g'_\theta \phi'^2 - 2\phi' K_{22} \frac{\pi}{p} sin\, 2\,\theta + \frac{1}{2}\varepsilon_a E_z^2\, sin\, 2\theta = 0,$$
$$\phi'' g + \phi'\theta' g'_\theta + \theta' K_{22} \frac{2\pi}{p} \sin 2\theta = 0. \quad (6)$$

Here, double primes denote the second derivatives with respect to z, and f'_θ and g'_θ denote the derivatives of $f(\theta)$ and $g(\theta)$ defined in (2) with respect to the angle θ. Solving equations (4, 6) along with the boundary conditions (3, 5) results in the equilibrium distributions of the director angles $\theta(z)$ and $\phi(z)$ and the potential $\Phi(z)$. Since the equations are nonlinear and strongly coupled, they can only be solved numerically.

Equilibrium director profiles

The distributions of the director angles θ and ϕ, and the potential Φ across the thickness of the LC cell for different values of the applied voltage U are presented in Fig. 2. Applying the voltage results in deformations in the $\theta(z)$ distribution as it is directly coupled with the local electric field, which in turn also causes the corresponding deformations in the angle $\phi(z)$. The resulting $\theta(z)$ profiles are symmetric, and the deviations of the $\phi(z)$ from the initial linear distribution are anti-symmetric with respect to the middle of the cell ($z = L/2$).

When the voltage reaches the value of around 1 V, the director angle deformations become sensitive to the voltage, which corresponds to a threshold-like behavior smoothed by the non-zero pretilt angle θ_0. Increasing the voltage to around 4V results in the director being oriented homeotropically in the bulk of the LC, while the boundary conditions at $z = 0$ and $z = L$ restrict complete reorientation.

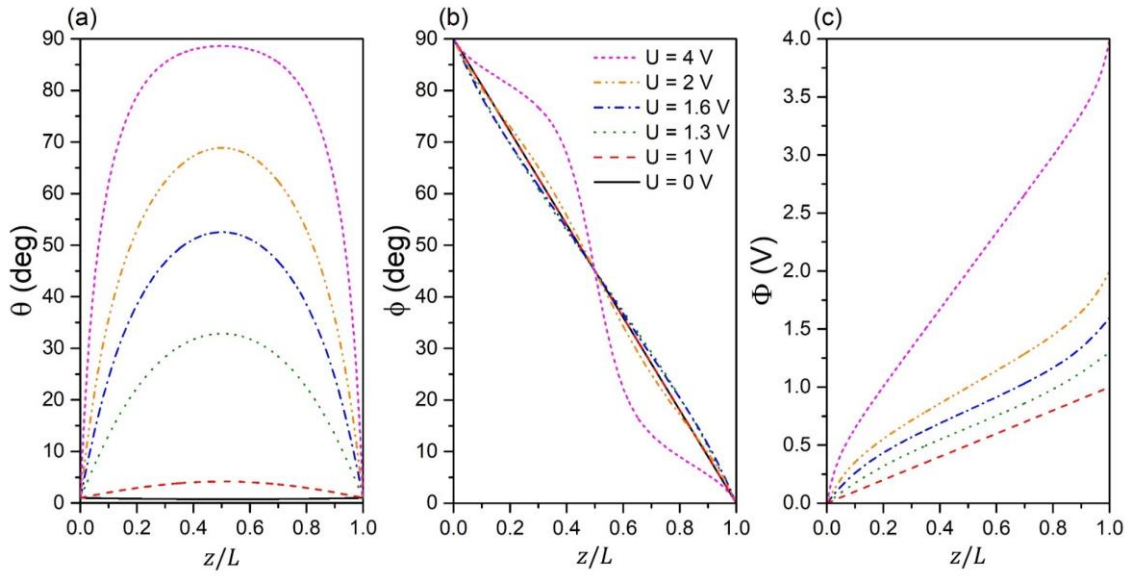

Figure 2. Distributions of director angles θ (a), ϕ (b), and the potential Φ (c) across the thickness of the LC cell.

At moderate voltages up to 2 V, the distribution of the director's ϕ angle remains almost linear. However, as the voltages increase, the $\phi(z)$ dependence becomes non-linear with an increasing inclination at the center of the cell and a decreased inclination closer to the boundaries. This is caused by the director aligning along the z axis in the center of the cell, thus making the ϕ angle more and more redundant, almost allowing for a discontinuity in the $\phi(z)$ distribution which would be possible at $\theta = \pi/2$.

For voltages lower than around 1 V, the potential profiles $\Phi(z)$ are roughly linear: $\Phi(z) \approx zU/L$ (Fig. 2c). However, as $\theta(z)$ starts to significantly deviate from a uniform distribution at higher voltages, the distribution of the potential across the thickness of the LC cell becomes non-linear.

Reflectance and absorbance spectra, near field enhancement

Reflectance and absorbance

The reflectance and absorbance spectra of the Yagi-Uda micro-antenna arrays for different applied voltage values are presented in Fig. 3. Reflectance and absorbance spectra in the 6–12 THz frequency range are represented by distinct dips and peaks, respectively, which correspond to different plasmonic resonant modes being excited in the Yagi-Uda antennas. Due to the presence of the metal film forming the ground plane (Fig. 1a), the transmittance in the studied structure is negligible, resulting in $R \approx 1 - A$ where R and A are reflectance and absorbance, respectively.

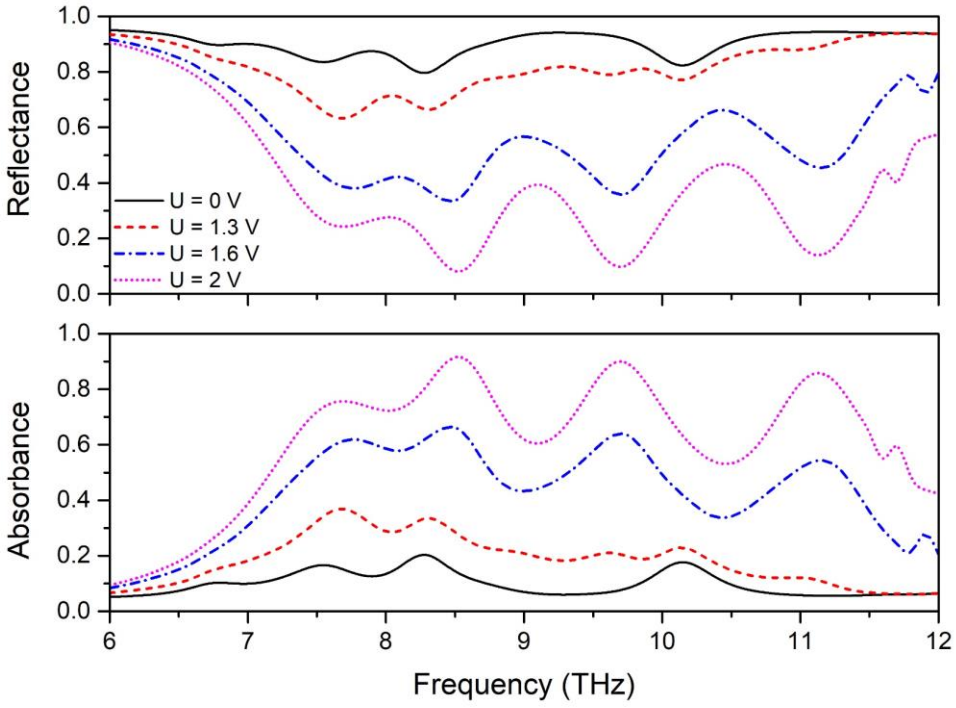

Figure 3. Reflectance and absorbance spectra for the values of 0, 1.3, 1.6, and 2 V of the applied voltage U.

While the incident wave is initially y-polarized, its polarization may change as it passes through the LC depending on the value of the applied voltage. Therefore, the term ‘local

polarization’ will be adopted to denote the wave's polarization state at its point of interaction with the Yagi-Uda antenna.

When no voltage is applied to the LC cell (Fig. 3, solid line), the absorbance profile has several weak peaks at 7.5, 8.3, and 10.1 THz reaching 20% in amplitude. Applying voltage to the LC cell disables the Mauguin regime, changing the local polarization. As a result, the absorbance increases by 50–60% on average, forming distinct peaks at 7.7, 8.5, 9.7, and 11.1 THz with an amplitude of up to 90% (Fig. 3, dotted line).

Near field distribution at $U = 0$ V

he gradual peaks at the frequencies f of 7.5, 8.3, and 10.1 THz at $U = 0$ V (Fig. 3, solid line) correspond to the resonances localized around different arms of the antenna. Fig. 4 shows the corresponding distributions of the electric field components. Here, the electric field is expressed in the units of the incident wave’s electric field norm.

Examining the individual components of the local electric field reveals that even if no voltage is applied, the excited modes have different symmetry at different frequencies. The mode at 10.1 THz has a symmetric E_x and antisymmetric E_y components with respect to the horizontal x-axis, and has a negligible E_z component. This is a signature symmetry of a mode excited by incident light with local x-polarization [46], which is in accordance with the expectation of initial y-polarized wave being rotated following the established Mauguin regime.

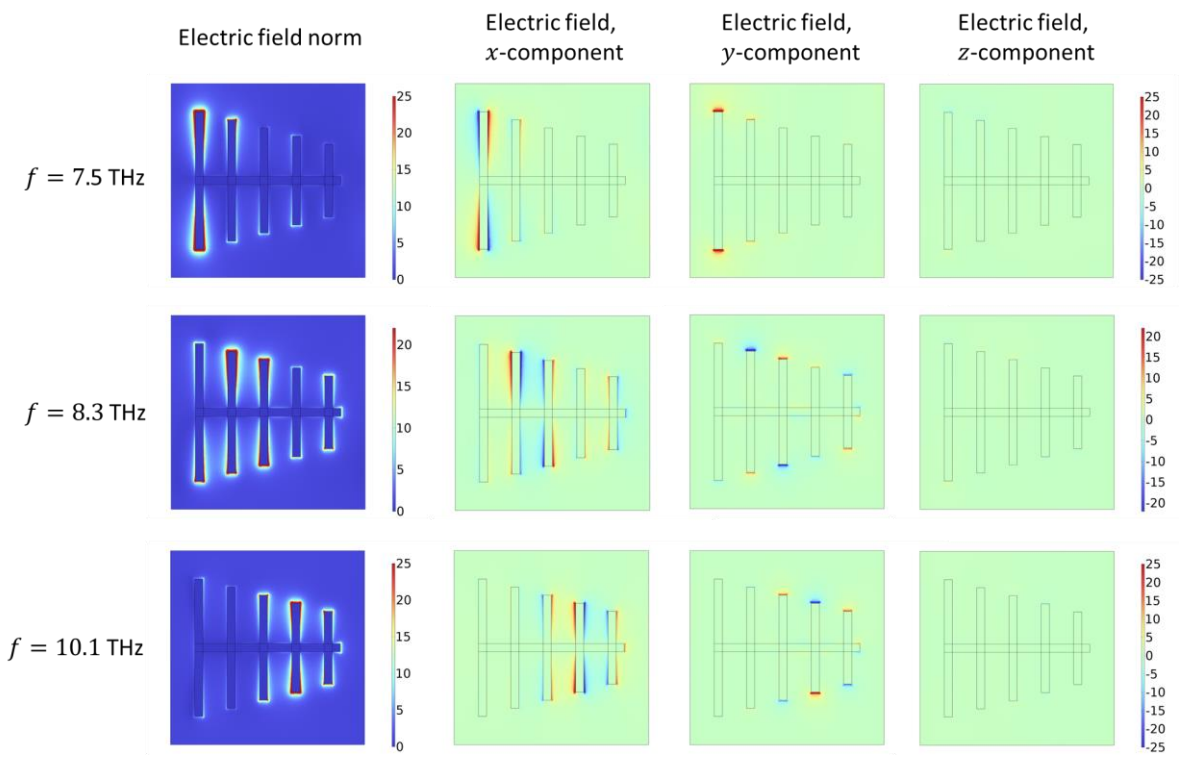

Figure 4. Distribution of the electric field components for $U = 0$ V near the Yagi-Uda antennas, expressed in the units of the incident wave's electric field norm.

However, not all resonances at the applied voltage of $U = 0$ V have such symmetry. Indeed, the peak at 7.5 THz is clearly much closer to having an antisymmetric E_x and symmetric E_y components with respect to the horizontal x-axis, which is characteristic of the incident light with the local y-polarization; this indicates that the Mauguin regime is at least partially disabled at this frequency due to it being sensitive to the frequency of the incident light. The 8.3 THz peak is indicative of an intermediate regime where the presence of both x- and y- components of the exciting wave results in a combination of the mentioned modes, forming an asymmetrical distribution of the electric field.

Near field distribution at $U = 2$ V

An increase of the voltage applied to the cell gradually reorients the LC director toward the homeotropic orientation. This results in the projection of the optical anisotropy on the

$x - y$ plane decreasing, gradually disabling the Mauguin regime. As such, the LCs' ability to rotate the polarization plane of the incident light weakens, resulting in the light reaching the Yagi-Uda antennas becoming closer to the initial polarization along the y-axis.

The distribution of the electric field components near the Yagi-Uda antenna, at the voltage $U = 2$ V, corresponding to the electric field strength of 40 kV m^{-1}, is presented in Fig. 5. The resonances, similar to the case of $U = 0$ V, are localized in the arms of the antennas. In the case of $U = 2$ V, all resonances have similar symmetry of the local electric field, which corresponds to the incident wave's local polarization being along the y-axis. This indicates that at $U = 2$ V the Mauguin regime is disabled and the light propagates through the LC without significant changes in polarization. It should be noted that there is no fundamental difference in symmetry between the modes at 9.7 and 11.1 THz. The observed inversion of all components' signs merely reflects that the electric field components' snapshots were captured at different phases of their oscillatory cycle.

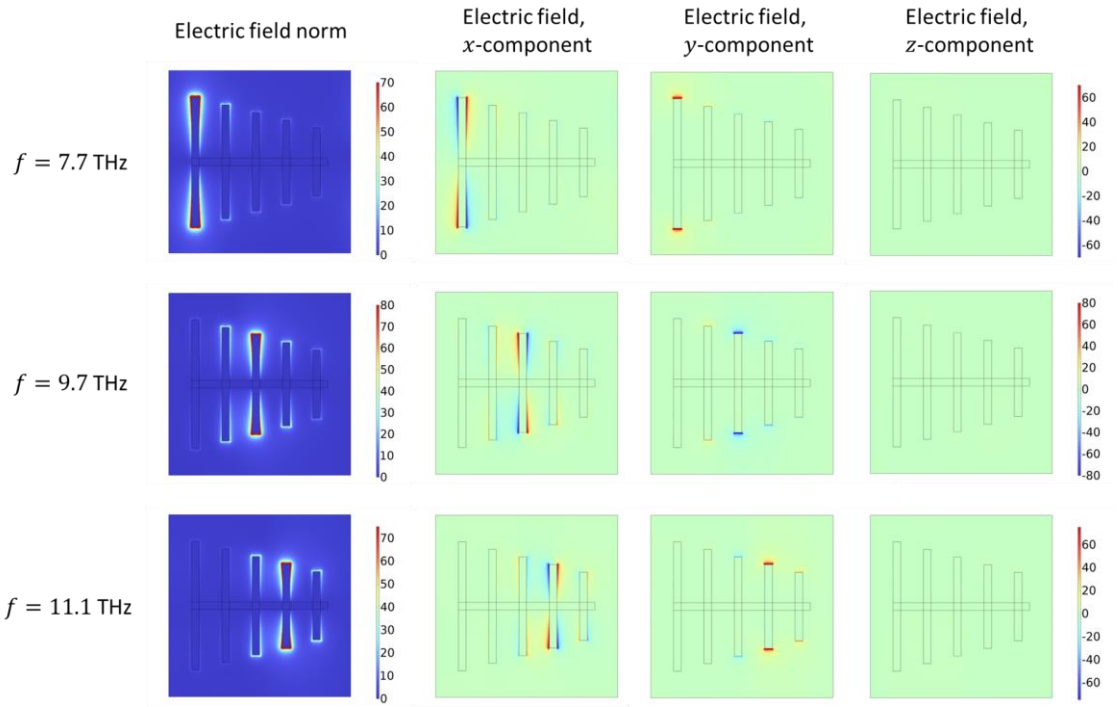

Figure 5. Distribution of the electric field components for $U = 2$ V near the Yagi-Uda antenna.

The absorbance contributions from different components of the system are detailed in Fig. 6 for a voltage of $U = 2$ V. Within the resonance peaks, the majority of absorbance is attributed to the Yagi-Uda antenna and the dielectric slab, a result of the resonances being localized near the antennas. Outside of resonance frequencies, absorbance significantly decreases, and the contributions from the Yagi-Uda antenna, dielectric layer, and the ground plane become comparable in magnitude.

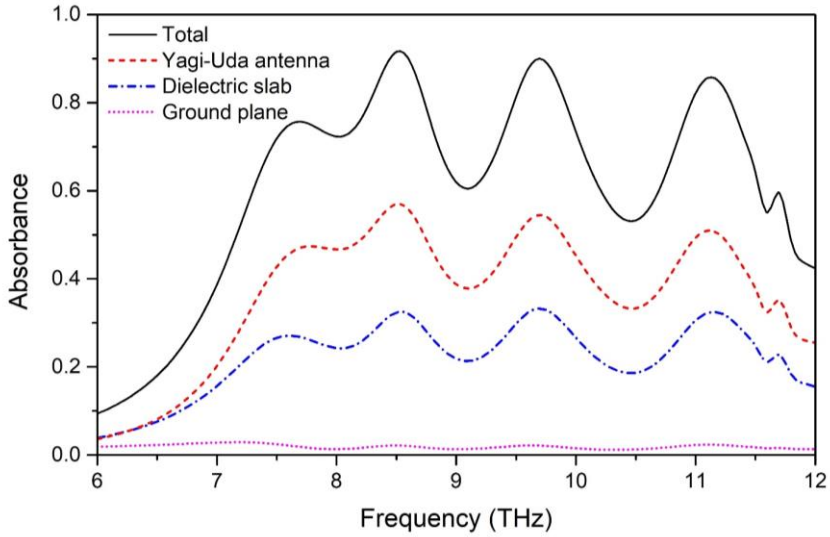

Figure 6. Breakdown of total absorbance at $U = 2$ V showing contributions from the Yagi-Uda antenna, dielectric slab, and ground plane.

Sensitivity to applied voltage

Figure 7 presents the distribution of the x-component of the electric field for three selected peaks of 7.7, 9.7, and 11.1 THz at different applied voltages. These peaks correspond to the resonances at $U = 2$ V (Fig. 3, dotted line). At a high voltage of 2 V, when the director is almost completely reoriented, the x-component of the electric field

is antisymmetric, indicating a clear correspondence to the excitation light's local polarization along the y-axis.

As the voltage decreases, asymmetries start to reveal, to the point that at $U = 0$ V there is no indication of any symmetry with respect to the x- axis, which is likely a result of superposition of different modes, since the excitation wave's local polarization has both x- and y- components. The selected frequencies of 7.7, 9.7, and 11.1 THz do not correspond to the resonance frequencies at $U = 0$ V (Fig. 3, solid line), resulting in a relatively weak near field enhancement (see Fig. 4 for comparison).

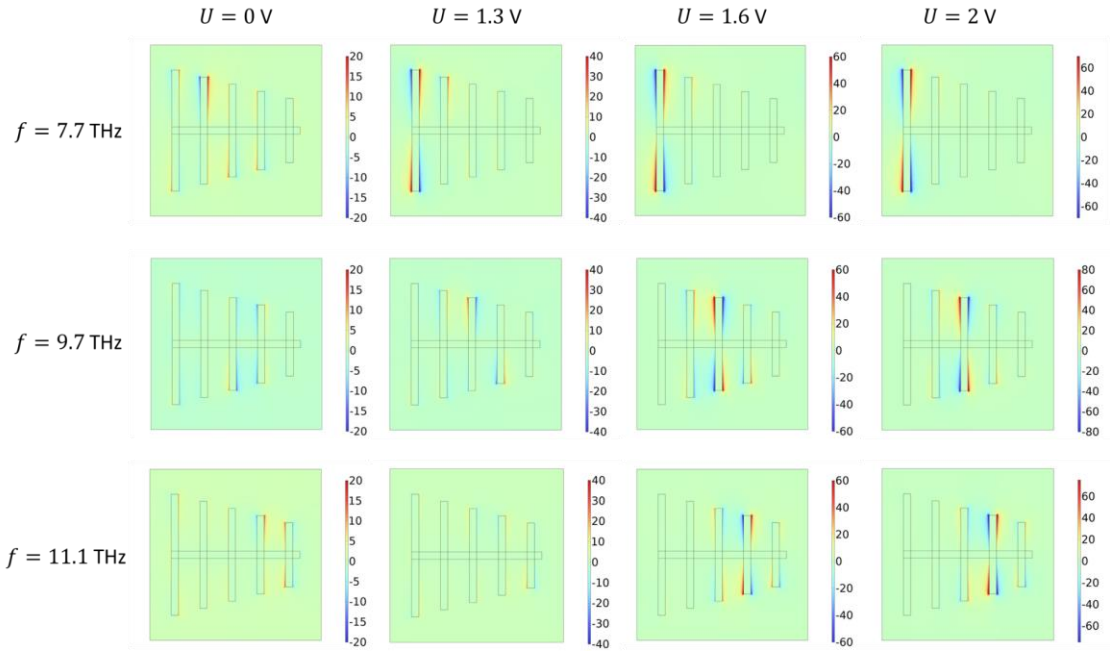

Figure 7. Evolution of the electric field's x-component at the frequencies of 7.7, 9.7, and 11.1 THz as the applied voltage increases.

Additionally, Fig. 7 hints that the resonances of higher frequencies start to form at higher voltages. To confirm this phenomenon, Fig. 8 presents the dependence of the mentioned resonances on the applied voltage. It is apparent that the transition region, while mostly being confined within 1–2 V range, shifts toward higher voltages as the frequency

increases. Additionally, it reveals that the reflectance can change with voltage with slight deviations from monotonicity: the 11.1 THz curve has a barely noticeable bump at approximately 1.2 V, and the 7.7 THz curve is very slightly increasing with voltage in the 2.5–3 V range. This deviation from the monotonicity is likely caused by the superposition of the decreasing monotonic contribution of disabling the Mauguin regime, and a much weaker increasing monotonic contribution of the resonances shifting due to director reorienting near the Yagi-Uda antennas.

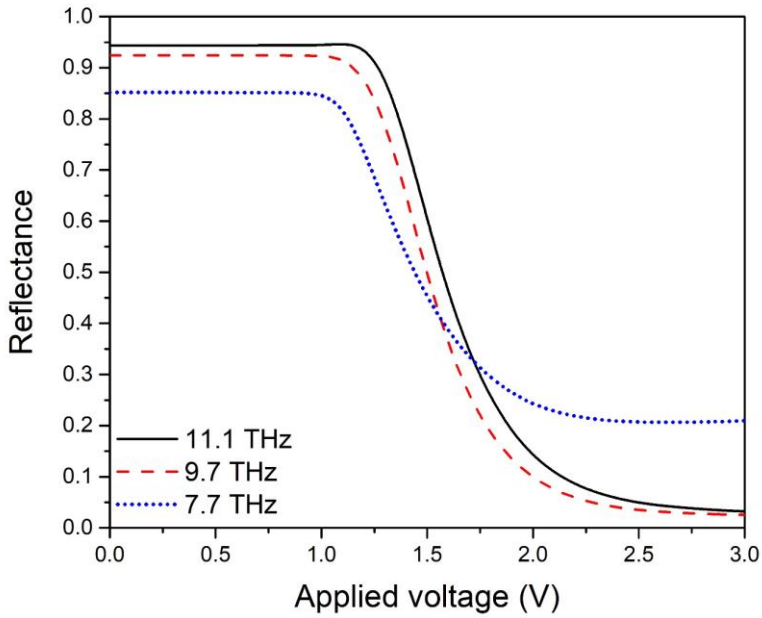

Figure 8. Dependence of the reflectance at 7.7, 9.7, and 11.1 THz on the applied voltage.

Overall, the absorbance and reflectance can be controlled over the broad frequency range of 7–12 THz, where the resonances associated with different antenna arms are excited. Since the transmittance of the studied structure is negligible due to the presence of the ground plane, the control ranges for reflectance and absorbance match. These ranges are on average around 50–60% in the mentioned frequency interval, reaching up to 80–90% at selected frequencies, i.e., 11.1 THz.

Discussion

The key mechanism for absorbance control in the presented structure is the absorbance sensitivity of the Yagi-Uda antenna array to the polarization of the incident THz wave. The role of the twisted nematic is to alter the polarization state of the incoming light when it reaches the Yagi-Uda antenna array plane. As a result, with different voltages applied to the LC cell, the incident light wave has different polarizations upon reaching the antenna array plane, allowing one to control the reflectance and absorbance spectra of the system by changing the applied voltage.

At a given voltage and a fixed LC director distribution across the cell, the increase in the frequency of the incident wave affects the reflectance and absorbance spectra in several ways. First, as the frequency increases, the resonances shift between different arms of the Yagi-Uda antennas. Starting from the largest arm at around 7.5 THz, the increase in frequency of the incident light leads to a gradual shift of the resonances toward the smaller arms. The local electric field enhancement is confined within one or a several adjacent arms, however strong resonances occur only when such confinement is centered around a single antenna arm.

The second way the change in the frequency of incident light affects the resonances is related to the fulfillment of the Mauguin regime condition

$$\beta = \frac{(n_e - n_o)|P|}{\lambda} \gg 1, \tag{7}$$

where P is the actual LC pitch, which matches the intrinsic LC pitch p for voltages $U \lesssim 2\,V$ (Fig. 2b), λ is the wavelength of the incident wave in vacuum, and β is the dimensionless parameter that provides a quantitative measure for the fulfillment of the Mauguin regime. Indeed, an increase in frequency means a decrease in the wavelength of

the light within the LC medium, better fulfilling the Mauguin regime condition (7); this is confirmed by analyzing the spatial symmetry of the electric field components' distribution (Fig. 4).

Reorienting the LC toward the homeotropic orientation can from one side be viewed as effectively decreasing the $(n_e - n_o)$ factor in the equation for the Mauguin regime criterion (7), thus decreasing the Mauguin regime fulfillment indicator β. On the other hand, director reorientation results in the change of the optical properties of the LC near the Yagi-Uda antennas. The former control channel is related to the bulk of the LC, as the Mauguin regime has to be established along the whole path of the incident light. The latter channel, however, is related to the director orientation near the antenna, as the resonance is most sensitive to the dielectric tensor in the regions of the strongest field enhancement.

Besides the expected polarization change of the incident light when it reaches the Yagi-Uda antennas, the change in the applied voltage can also lead to sophisticated effects when its action is regarded in context of the frequency-dependence of the Mauguin regime fulfillment criterion. Since $\beta_{12THz} \approx 2\beta_{6THz}$, the Mauguin regime at higher frequencies can still hold, even if the director profile starts to deviate from the optimal $\pi/2$ twisted distribution, becoming less sensitive to the voltage changes for relatively low voltages (Fig. 8). The decrease in sensitivity in the 1–1.3 V range at $f = 11.1\ THz$ is then compensated by an increased sensitivity to the voltages around 1.3–1.8 V. Overall, the presented structure provides better opportunities for lower-voltage control of reflectance and absorbance in the 7–8 THz frequency interval, while at higher frequencies, the voltages of around 1.7 V are best for achieving significant control over the reflectance and absorbance.

Conclusion

We have successfully demonstrated how LCs can be utilized to precisely adjust the resonance characteristics of Yagi-Uda micro-antenna arrays. The design of a LC-controlled Yagi-Uda micro-antenna array is presented, where altering the orientation of the LC enables the manipulation of both absorbance and reflectance within the frequency range of 7–12 THz. This method allows for an average absorbance and reflectance control of 50–60% across the 7–12 THz interval, with a peak effectiveness of approximately 90% at 11 THz. The operating voltages are found to be approximately 1.1–1.9 V for lower frequencies (~7 THz), and 1.4–2.5 V for higher frequencies (~11 THz). This research broadens the scope for employing LCs to dynamically enhance and control the resonance features of Yagi-Uda metamaterial absorbers, expanding the potential for real-time modulation of their properties.

The authors declare no competing interests.

References

1. Smith DR, Padilla WJ, Vier DC, Nemat-Nasser SC, Schultz S. Composite Medium with Simultaneously Negative Permeability and Permittivity. Phys Rev Lett. 2000;84:4184–4187. doi: 10.1103/physrevlett.84.4184.
2. Wang S, Liu H, Tang J, Chen M, Zhang Y, Xu J, Wang T, Xiong J, Wang H, Cheng Y, et al. Tunable and switchable bifunctional meta-surface for plasmon-induced transparency and perfect absorption. Opt Mater Express. 2022;12:560. doi: 10.1364/ome.449748.
3. Carroll JE. Metamaterials: Critique and Alternatives, by B.A. Munk. Contemp Phys. 2010;51:441–444. doi: 10.1080/00107510903298206.
4. Donzelli G, Vallecchi A, Capolino F, Schuchinsky A. Metamaterial made of paired planar conductors: Particle resonances, phenomena and properties. Metamaterials. 2009;3:10–27. doi: 10.1016/j.metmat.2008.12.001.

5. Ra'di Y, Simovski CR, Tretyakov SA. Thin Perfect Absorbers for Electromagnetic Waves: Theory, Design, and Realizations. Phys Rev Appl. 2015;3. doi: 10.1103/physrevapplied.3.037001.
6. Schurig D, Mock JJ, Justice BJ, Cummer SA, Pendry JB, Starr AF, Smith DR. Metamaterial Electromagnetic Cloak at Microwave Frequencies. Science. 2006;314:977–980. doi: 10.1126/science.1133628.
7. Reshetnyak VYu, Pinkevych IP, Sluckin TJ, Evans DR. Cloaking by shells with radially inhomogeneous anisotropic permittivity. Opt Express. 2015;24:A21. doi: 10.1364/oe.24.000a21.
8. Pendry JB. Negative Refraction Makes a Perfect Lens. Phys Rev Lett. 2000;85:3966–3969. doi: 10.1103/physrevlett.85.3966.
9. Burgos SP, de Waele R, Polman A, Atwater HA. A single-layer wide-angle negative-index metamaterial at visible frequencies. Nat Mater. 2010;9:407–412. doi: 10.1038/nmat2747.
10. Wen Q-Y, Zhang H-W, Yang Q-H, Chen Z, Long Y, Jing Y-L, Lin Y, Zhang P-X. A tunable hybrid metamaterial absorber based on vanadium oxide films. J Phys D: Appl Phys. 2012;45:235106. doi: 10.1088/0022-3727/45/23/235106.
11. Chen W-C, Mock JJ, Smith DR, Akalin T, Padilla WJ. Controlling Gigahertz and Terahertz Surface Electromagnetic Waves with Metamaterial Resonators. Phys Rev X. 2011;1. doi: 10.1103/physrevx.1.021016.
12. Soukoulis CM, Wegener M. Past achievements and future challenges in the development of three-dimensional photonic metamaterials. Nat Photonics. 2011;5:523–530. doi: 10.1038/nphoton.2011.154.
13. McPhedran RC, Shadrivov IV, Kuhlmey BT, Kivshar YS. Metamaterials and metaoptics. NPG Asia Mater. 2011;3:100–108. doi: 10.1038/asiamat.2011.146.
14. Yang S, Liu P, Yang M, Wang Q, Song J, Dong L. From Flexible and Stretchable Meta-Atom to Metamaterial: A Wearable Microwave Meta-Skin with Tunable Frequency Selective and Cloaking Effects. Sci Rep. 2016;6. doi: 10.1038/srep21921.
15. Matsui T, Taniguchi S, Yoshida K, Murata H. Reflection-less frequency-selective microwave metamaterial absorber. OSA Continuum. 2021;4:2351. doi: 10.1364/osac.432737.
16. Yang P-A, Huang Y, Li R, Huang X, Ruan H, Shou M, Li W, Zhang Y, Li N, Dong L. Optimization of Fe@Ag core–shell nanowires with improved impedance

matching and microwave absorption properties. Chem Eng J. 2022;430:132878. doi: 10.1016/j.cej.2021.132878.

17. Krasnok A, Baranov D, Li H, Miri M-A, Monticone F, Alú A. Anomalies in light scattering. Adv Opt Photonics. 2019;11:892. doi: 10.1364/aop.11.000892.
18. Naveed MA, Ansari MA, Kim I, Badloe T, Kim J, Oh DK, Riaz K, Tauqeer T, Younis U, Saleem M, et al. Optical spin-symmetry breaking for high-efficiency directional helicity-multiplexed metaholograms. Microsyst Nanoeng. 2021;7. doi: 10.1038/s41378-020-00226-x.
19. Damasceno GHB, Carvalho WOF, Mejía-Salazar JR. Design of Plasmonic Yagi–Uda Nanoantennas for Chip-Scale Optical Wireless Communications. Sensors. 2022;22:7336. doi: 10.3390/s22197336.
20. Sol J, Smith DR, del Hougne P. Meta-programmable analog differentiator. Nat Commun. 2022;13. doi: 10.1038/s41467-022-29354-w.
21. Valipour A, Kargozarfard MH, Rakhshi M, Yaghootian A, Sedighi HM. Metamaterials and their applications: An overview. Proc Inst Mech Eng, Part L: J Mater: Des Appl. 2021;236:2171–2210. doi: 10.1177/1464420721995858.
22. Hussain M, Awan WA, Alzaidi MS, Hussain N, Ali EM, Falcone F. Metamaterials and Their Application in the Performance Enhancement of Reconfigurable Antennas: A Review. Micromachines. 2023;14:349. doi: 10.3390/mi14020349.
23. Cui TJ. Microwave metamaterials. Natl Sci Rev. 2017;5:134–136. doi: 10.1093/nsr/nwx133.
24. Wu X, Eleftheriades GV, van Deventer-Perkins TE. Design and characterization of single- and multiple-beam mm-wave circularly polarized substrate lens antennas for wireless communications. IEEE Trans Microwave Theory Tech. 2001;49:431–441. doi: 10.1109/22.910546.
25. Kolb PW, Salter TS, McGee JA, Drew HD, Padilla WJ. Extreme subwavelength electric GHz metamaterials. J Appl Phys. 2011;110. doi: 10.1063/1.3633213.
26. Bilal RMH, Baqir MA, Choudhury PK, Ali MM, Rahim AA. On the specially designed fractal metasurface-based dual-polarization converter in the THz regime. Results Phys. 2020;19:103358. doi: 10.1016/j.rinp.2020.103358.
27. Asadchy VS, Faniayeu IA, Ra'di Y, Khakhomov SA, Semchenko IV, Tretyakov SA. Broadband Reflectionless Metasheets: Frequency-Selective Transmission and Perfect Absorption. Phys Rev X. 2015;5. doi: 10.1103/physrevx.5.031005.

28. F. Imani M, Smith DR, del Hougne P. Perfect Absorption in a Disordered Medium with Programmable Meta‐Atom Inclusions. Adv Funct Mater. 2020;30. doi: 10.1002/adfm.202005310.
29. Landy NI, Sajuyigbe S, Mock JJ, Smith DR, Padilla WJ. Perfect Metamaterial Absorber. Phys Rev Lett. 2008;100. doi: 10.1103/physrevlett.100.207402.
30. Huang X, He W, Yang F, Ran J, Gao B, Zhang W-L. Polarization-independent and angle-insensitive broadband absorber with a target-patterned graphene layer in the terahertz regime. Opt Express. 2018;26:25558. doi: 10.1364/oe.26.025558.
31. Chen F, Cheng Y, Luo H. A Broadband Tunable Terahertz Metamaterial Absorber Based on Single-Layer Complementary Gammadion-Shaped Graphene. Materials. 2020;13:860. doi: 10.3390/ma13040860.
32. Cheng Y, Chen F, Luo H. Plasmonic Chiral Metasurface Absorber Based on Bilayer Fourfold Twisted Semicircle Nanostructure at Optical Frequency. Nanoscale Res Lett. 2021;16. doi: 10.1186/s11671-021-03474-6.
33. Bilal RMH, Baqir MA, Choudhury PK, Naveed MA, Ali MM, Rahim AA. Ultrathin broadband metasurface-based absorber comprised of tungsten nanowires. Results Phys. 2020;19:103471. doi: 10.1016/j.rinp.2020.103471.
34. Bilal RMH, Baqir MA, Hameed M, Naqvi SA, Ali MM. Triangular metallic ring-shaped broadband polarization-insensitive and wide-angle metamaterial absorber for visible regime. J Opt Soc Am A. 2021;39:136. doi: 10.1364/josaa.444523.
35. Yang P, Ruan H, Sun Y, Li R, Lu Y, Xiang C. Excellent microwave absorption performances of high length-diameter ratio iron nanowires with low filling ratio. Nanotechnology. 2020;31:395708. doi: 10.1088/1361-6528/ab9d41.
36. Wang Q, Cheng Y. Compact and low-frequency broadband microwave metamaterial absorber based on meander wire structure loaded resistors. AEU Int J Electron Commun. 2020;120:153198. doi: 10.1016/j.aeue.2020.153198.
37. Maksymov IS, Staude I, Miroshnichenko AE, Kivshar YS. Optical Yagi-Uda nanoantennas. Nanophotonics. 2012;1:65–81. doi: 10.1515/nanoph-2012-0005.
38. Pattanayak A, Roy S, Rana G, Duttagupta SP, Achanta VG, Prabhu SS. Study of THz-Plasmon hybridization of a loop Yagi-Uda absorber. Sci Rep. 2017;7. doi: 10.1038/s41598-017-17311-3.
39. Bilal RMH, Baqir MA, Iftikhar A, Naqvi SA, Mughal MJ, Ali MM. Polarization-controllable and angle-insensitive multiband Yagi-Uda-shaped metamaterial

absorber in the microwave regime. Opt Mater Express. 2022;12:798. doi: 10.1364/ome.451073.

40. Pratibha R, Park K, Smalyukh II, Park W. Tunable optical metamaterial based on liquid crystal-gold nanosphere composite. Opt Express. 2009;17:19459. doi: 10.1364/oe.17.019459.
41. Xu J, Yang R, Fan Y, Fu Q, Zhang F. A Review of Tunable Electromagnetic Metamaterials With Anisotropic Liquid Crystals. Front Phys. 2021;9. doi: 10.3389/fphy.2021.633104.
42. Zhou S, Shen Z, Kang R, Ge S, Hu W. Liquid Crystal Tunable Dielectric Metamaterial Absorber in the Terahertz Range. Appl Sci. 2018;8:2211. doi: 10.3390/app8112211.
43. Reshetnyak VYu, Pinkevych IP, Urbas AM, Evans DR. Controlling hyperbolic metamaterials with a core-shell nanowire array [Invited]. Opt Mater Express. 2017;7:542. doi: 10.1364/ome.7.000542.
44. Abu Aisheh M, Abutoama M, Abuleil MJ, Abdulhalim I. Fast tunable metamaterial liquid crystal achromatic waveplate. Nanophotonics. 2023;12:1115–1127. doi: 10.1515/nanoph-2022-0656.
45. Lv J-F, Meng F-Y, Zhang K, Han J-Q, Liu Y-H, Ding C, Wu Q. Tunable liquid crystal metamaterial filter with polarization-insensitive characteristic. Liq Cryst. 2022;49:1338–1346. doi: 10.1080/02678292.2022.2031325.
46. Yakovkin I, Reshetnyak V. Liquid crystal-enabled tunability of Yagi-Uda antenna resonant properties. J Opt Microsyst. 2023;3. doi: 10.1117/1.jom.3.4.041203.
47. Du Y, Tian H, Cui X, Wang X, Lu J, Zhou Z. Super terahertz transparent electrodes. Opt Express. 2016;24:6359. doi: 10.1364/oe.24.006359.
48. Arakawa Y, Kang S, Tsuji H, Watanabe J, Konishi G. The design of liquid crystalline bistolane-based materials with extremely high birefringence. RSC Adv. 2016;6:92845–92851. doi: 10.1039/c6ra14093a.
49. Dąbrowski R, Kula P, Herman J. High Birefringence Liquid Crystals. Crystals. 2013;3:443–482. doi: 10.3390/cryst3030443.
50. Ordal MA, Bell RJ, Alexander RW, Long LL, Querry MR. Optical properties of fourteen metals in the infrared and far infrared: Al, Co, Cu, Au, Fe, Pb, Mo, Ni, Pd, Pt, Ag, Ti, V, and W. Appl Opt. 1985;24:4493. doi: 10.1364/ao.24.004493.
51. Pasunoori P, Engin AE. Automated dielectric constant and loss tangent characterization using cavity resonators. 2011 IEEE International Symposium on

Electromagnetic Compatibility; 2011; Long Beach, CA; 2011;doi: 10.1109/isemc.2011.6038365.

52. Chao PC-P, Kao Y-Y, Hsu C-J. A new negative liquid crystal lens with multiple ring electrodes in unequal widths. IEEE Photonics J. 2012;4:250–266. doi: 10.1109/jphot.2012.2183583.
53. Yang D-K, Wu S-T. Fundamentals of Liquid Crystal Devices. John Wiley & Sons; 2014.